Numerical investigation of spallation neutrons generated from petawatt-scale laserdriven proton beams

B Martinez, S N Chen, S Bolaños, N Blanchot, G Boutoux, W Cayzac, C Courtois, X Davoine, A Duval, V Horny, et al.

Numerical investigation of spallation neutrons generated from petawatt-scale laser-driven proton beams

B. Martinez[1,2*], S. N. Chen[3], S. Bolaños[1], N. Blanchot[4], G. Boutoux[2], W. Cayzac[2], C. Courtois[2], X. Davoine[2,5], A. Duval[2], V. Horny[1,2], I. Lantuejoul[2], L. Le Deroff[4], P. E. Masson-Laborde[2,5], G. Sary[2,5], B. Vauzour[2], R. Smets[6], L. Gremillet[2,5, †], J. Fuchs[1, §]

1. LULI-CNRS, CEA, UPMC Univ Paris 06: Sorbonne Université, Ecole Polytechnique, Institut Polytechnique de Paris – F-91128 Palaiseau Cedex, France
2. CEA, DAM, DIF, F-91297 Arpajon, France
3. Horia Hulubei National Institute of Physics and Nuclear Engineering, Bucharest – Magurele, Romania
4. CEA, DAM, CESTA, F-33114 Le Barp, France
5. Université Paris-Saclay, CEA, LMCE, 91680 Bruyères-le-Châtel, France
6. LPP, Sorbonne Université, CNRS, Ecole Polytechnique, F-91128 Palaiseau, France

* bertrand.martinez@tecnico.ulisboa.pt; Present address: GoLP/Instituto de Plasmas e Fusão Nuclear, Instituto Superior Técnico, Universidade de Lisboa, Lisbon, Portugal
† laurent.gremillet@cea.fr
§ julien.fuchs@polytechnique.edu

Abstract

Laser-driven neutron sources could offer a promising alternative to those based on conventional accelerator technologies in delivering compact beams of high brightness and short duration. We examine this through particle-in-cell and Monte Carlo simulations, that model, respectively, the laser acceleration of protons from thin-foil targets and their subsequent conversion into neutrons in secondary lead targets. Laser parameters relevant to the 0.5 petawatt (PW) LMJ-PETAL and 0.6-6 PW Apollon systems are considered. Due to its high intensity, the 20-fs-duration 0.6 PW Apollon laser is expected to accelerate protons up to above 100 MeV, thereby unlocking efficient neutron generation via spallation reactions. As a result, despite a 30-fold lower pulse energy than the LMJ-PETAL laser, the 0.6 PW Apollon laser should perform comparably well both in terms of neutron yield and flux. Notably, we predict that very compact neutron sources, of ~ 10 ps duration and ~ 100 µm spot size, can be released provided the lead convertor target is thin enough (~ 100 µm). These sources are characterized by extreme fluxes, of the order of 10^{23} n cm^{-2} s^{-1}, and even ten times higher when using the 6 PW Apollon laser. Such values surpass those currently achievable at large-scale accelerator-based neutron sources (~ 10^{16} n cm^{-2} s^{-1}), or reported from previous laser experiments using low-*Z* converters (~ 10^{18} n cm^{-2} s^{-1}). By showing that such laser systems can produce neutron pulses significantly brighter than existing sources, our findings open a path towards attractive novel applications, such as flash neutron radiography or laboratory studies of heavy-ion nucleosynthesis.

1. Introduction

Neutron beams are commonly employed in research, medicine and industry for a wide range of applications [1]. In practice, they are generated from nuclear reactions initiated by accelerator proton beams. Conventional neutron source facilities range from compact tubes to large-scale linacs like the Spallation Neutron Source (Oak Ridge, USA) [2] or the European

Spallation Source (Lund, Sweden) [3] currently under construction, where $1-2$ GeV protons are hitting a heavy metal target to produce neutrons through spallation reactions. These consist of a cascade of binary collisions between the incident projectile and the nucleons inside the target nuclei, followed by de-excitation (or *evaporation*) of the excited nuclei, leading to the emission of neutrons, but also, to a smaller extent, protons, alpha particles, light heavy ions, gamma rays, etc. [4].

The production of bright neutron beams using high-power, short-pulse lasers was demonstrated in the early 2000's (see Ref. [5] and references therein for an overview) and has since been actively investigated. Laser-generated neutrons have already been utilized for a variety of purposes, such as material testing for fusion experiments [6], non-destructive imaging [7], and studies of equations of state via neutron resonance spectroscopy [8,9]. Such neutron sources exploit either laser-driven energetic protons [10] (with current record-high energies of ~ 100 MeV [11,12]), electrons [14] or gamma-ray photons [15] as the primary driver, with typical cross sections in the barn range [5,16] Most previous studies on this topic were focused on improving the yield [12,14] and the energy spectrum [17] of the emitted neutrons.

Progress in high-brightness neutron sources is a necessary step towards the laboratory production of neutron-rich isotopes via rapid neutron captures (*r*-process), which would allow nuclear physics models to be tested [18] and improve our understanding of the formation of heavy nuclei in the Universe [19,20]. Half of the elements heavier than Iron ($Z = 26$), and all those beyond Bismuth ($Z = 83$), are indeed believed to originate from the *r*-process during cataclysmic astrophysical events, e.g., supernova explosions or neutron star mergers [21]. In order to compensate for the short lifespan (in the ms range) of the intermediate isotopes, a minimum neutron flux $> 10^{20}$ n cm^{-2} s^{-1} is estimated for the r-process to operate [22]. This value is several orders of magnitude above the capability of conventional accelerator-based facilities ($\sim 10^{16}$ n cm^{-2}s^{-1}) [23], but also significantly larger than the current record-high flux ($\sim 10^{18}$ n cm^{-2}s^{-1}) obtained with intense short-pulse lasers [12,14]. Neutron fluxes as high as $\sim 10^{24}$ n cm^{-2}s^{-1} can be attained at large-scale laser fusion facilities [24], yet with limited user access and very few shots per experiment. Systematic laboratory investigations of *r*-process nucleosynthesis therefore require laser-based neutron sources to be further developed.

Laser acceleration of proton beams should greatly benefit from next-generation petawatt (PW) or multi-petawatt facilities, delivering pulse intensities in excess of 10^{21} Wcm^{-2} [25,26,27,28,29,30,31,32]. At such intensities, the dominant ion acceleration mechanism is expected to transition from target normal sheath acceleration (TNSA) [33] to radiative pressure acceleration (RPA) or light-sail acceleration (LSA) [34]. The accompanying increase in proton energy above the 100 MeV level should trigger spallation reactions in a secondary neutron-producing target, entailing the emission of multiple neutrons per incident proton (see Figure 1).

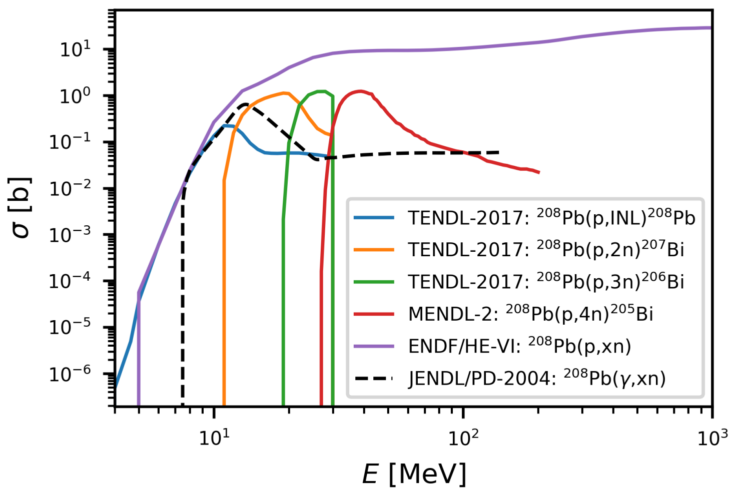

Figure 1: Energy-differential cross sections of proton-induced nuclear reactions releasing different numbers of neutrons (solid curves) and of total neutron production by photonuclear reactions (black dashed curve) in Pb, as given by the ENDF/B-VIII database [35].

In Figure 1, the cross sections of various neutron-producing reactions (as given by the ENDF/B-VIII database [35]) are plotted as a function of the projectile (proton or photon) energy (solid lines). Already at relatively low proton energies of tens of MeV, easily produced by current high-intensity laser facilities, neutrons are efficiently produced. Then, to access the reactions with increased neutron multiplicity, it is clear that higher projectile energies are needed.

In the present study, we will focus on exploiting protons as a driver to induce the desired neutron beam. This is justified because the cross sections of photonuclear reactions in lead (black dashed curve), although comparable with those of proton-induced reactions around 10 MeV, are 100 times lower at higher energy. Thus, integrating the expected production of neutrons, induced by either photons or protons, in the cases that will be addressed of the LMJ-PETAL [36] and Apollon [37] laser facilities, shows that the neutron yield induced by protons is at least ten times higher than that due to photons. The characteristics of the proton beams considered here will be detailed below, while to estimate the photons that can be generated by PETAL (resp. Apollon), we refer to Ref. [38] (resp. [39,40]). Hence, photonuclear reactions will be neglected in a first-order approach in the physical situations treated in the following. Yet, these could prove to be influential at more extreme laser intensities ($\geq 10^{23}$ W. cm^{-2}, not presently achievable) for which massive high-energy synchrotron radiation is expected to arise [40,41].

This paper reports on a numerical study aiming to characterize the neutron yield and flux achievable at the petawatt-class LMJ-PETAL and Apollon laser facilities. Our results are also relevant to similar laser systems, such as ELI-beamlines [42] or ELI-NP [43]. Overall, this is done by combining particle-in-cell (PIC) simulations of the laser-driven particle acceleration in a thin-foil target with Monte Carlo calculations of the proton-induced nuclear reactions in a secondary target. In Section 2, we first investigate numerically how the production of spallation neutrons varies with the target material and incident proton energy. In Section 3, we present the results of PIC simulations of laser-based proton acceleration from solid foils under conditions accessible at LMJ-PETAL and Apollon. The generation of spallation neutrons from a lead convertor by the PIC-predicted proton beams is studied via Monte Carlo simulations in Sec. 4, which predict that neutron yields of $10^8 - 10^{11}$ n str^{-1} and neutron fluxes of $10^{23} - 10^{24}$ n cm^{-2}s^{-1} are achievable. Finally, our results are summarized and discussed in Sec. 5.

2. Dependence of neutron production on target material and proton energy

Proton energy (MeV)	Al	Cu	Ag	Pb
25	0.315	0.117	0.115	0.135
50	1.08	0.391	0.380	0.435
100	3.70	1.31	1.26	1.43
250	17.9	6.28	5.97	6.64
500	55.0	19.1	18.1	19.9
1000	152	52.9	49.7	54.2

Table 1: Projected range λ (cm) for protons in various materials and for various energies.

We start by briefly examine the neutron yield from spallation as a function of the converter target material and the projectile proton energy in a range within the reach of present or near-future laser systems [11,34]. For this purpose, we have used the FLUKA 3D Monte Carlo code [44,45] to simulate the nuclear reactions induced during irradiation of a convertor target by a mono-kinetic and mono-directional proton beam. The proton beam energy was varied from $\epsilon_p = 25$ MeV to 1 GeV. Four target materials were considered: aluminum ($Z = 13$), copper ($Z = 29$), silver ($Z = 47$), and lead ($Z = 82$), a standard material for spallation purposes.

The simulated target was a 50 cm-radius cylinder of variable length L. Introducing λ the energy-dependent projected range of a proton due to ionization and excitation [46], five L/λ values (0.2,0.4,0.6,0.8,1) were considered for each material and input proton energy. The values of λ corresponding to our parameter range are given in Table 1.

Figure 2 shows the L/λ dependence of the neutron multiplicity M_n, i.e., the number of neutrons produced per incident proton as a function of its input energy ϵ_p, for the different materials under consideration. Collisional stopping and scattering of the projectiles and product neutrons are taken into account in these simulations. The main result is that, whatever the material, M_n rises sharply (i.e. approximately quadratically) with ϵ_p when L/λ is kept constant. In Ag and Pb, M_n approaches unity (a usual criterion for the onset of spallation) for $\epsilon_p \simeq 250$ MeV and $L/\lambda \lesssim 1$. At higher ϵ_p, $M_n \geq 1$ can be achieved in lower L/λ targets. The maximum neutron multiplicity ($M_n \sim 10$) is obtained in Pb with $\epsilon_p = 1$ GeV and $L/\lambda = 0.4 - 0.6$. It should be noted that the increasing trend of M_n with ϵ_p ceases beyond $\epsilon_p \simeq 0.5 - 1$ GeV when $L/\lambda \gtrsim 0.5$. This is a known behavior in spallation studies, ascribed to the increasingly significant contribution of pion production to proton energy losses [4].

At fixed proton energy, M_n is predicted to rise by a relatively modest ($\sim 3\times$) factor when the normalized target thickness is increased from $L/\lambda = 0.2$ to 1. Finally, at fixed $\epsilon_p \leq 0.5$ GeV and L/λ, M_n shows a moderate increase with the atomic number, that is, a $\sim 3\times$ enhancement between Al and Pb. At $\epsilon_p = 1$ GeV, however, an approximate $10\times$ enhancement is obtained.

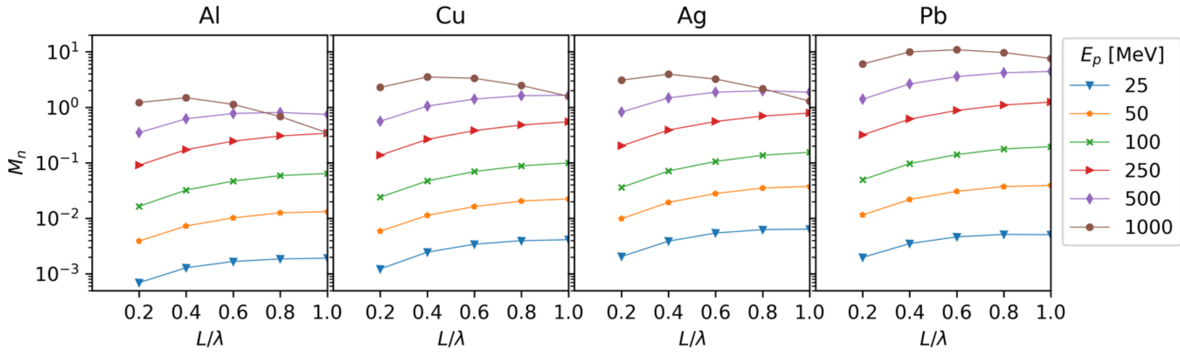

Figure 2: Number of neutrons emitted per incident proton as a function of the target material and incident proton energy, as simulated by FLUKA.

3. PIC simulations of laser acceleration of protons

We now numerically characterize the neutron beams that could be produced through spallation reactions in the near future, using the LMJ-PETAL and Apollon laser systems. Our methodology comprises two steps. First, we have employed the CALDER code [47] to perform multidimensional PIC simulations of proton acceleration from laser-irradiated foil targets, under conditions relevant to the LMJ-PETAL and Apollon lasers, as detailed in Table 2. Second, the proton distributions recorded in the PIC simulations have been used as input in 3D FLUKA Monte Carlo simulations [45], describing the proton transport and associated nuclear reactions through a secondary Pb convertor target. This procedure is sketched in Figure 3. In this Section, we present the results of the proton acceleration simulations for the LMJ-PETAL and Apollon cases.

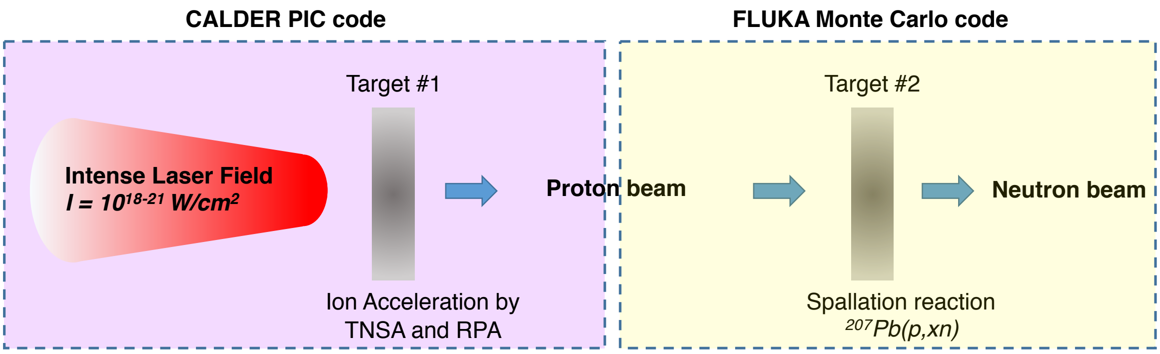

Figure 3: Conceptual setup of the numerical study.

Laser	Wavelength	Pulse duration	Pulse energy	Pulse intensity	Target size and composition	Simulation mesh size
0.5 PW LMJ-PETAL	1 µm	610 fs	320 J	8×10^{18} W/cm^2	5 µm CH & Al	32 nm
0.6 PW Apollon	0.8 µm	20 fs	12 J	2×10^{21} W/cm^2	64 nm CH	3.2 nm
6 PW	0.8 µm	20 fs	120 J	2×10^{22} W/cm^2	192 nm CH	3.2 nm

Apollon						

Table 2: Parameters of the 2D CALDER PIC simulations performed for each considered laser system.

3.1 Proton acceleration at the 0.5 PW LMJ-PETAL laser facility

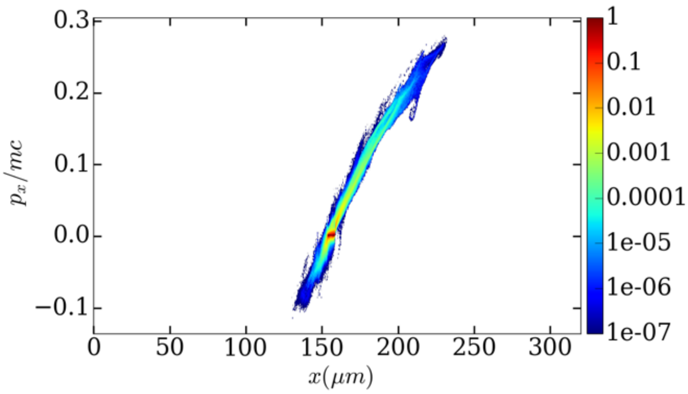

Figure 4: Longitudinal ($x - p_x$) phase space of the protons from the CALDER-CIRC simulation using the LMJ-PETAL parameters.

Proton acceleration using LMJ-PETAL was investigated in quasi-3D geometry with the CALDER-CIRC PIC code [48]. In this code, the particles are advanced in 3D Cartesian space but the fields and particle densities are computed in cylindrical coordinates (x, r, θ), using a reduced number of Fourier angular modes (only two angular modes were used here). This technique allows one to describe both the axisymmetric self-generated plasma fields (such as the TNSA field) and the non-axisymmetric (linearly polarized) laser fields at a much lower computational cost than in a fully 3D simulation. Based on experimental measurements [49], the PETAL laser beam was modeled as the sum of two superimposed, time-synchronized Gaussian laser waves, each of 610 fs FWHM duration, polarized along the y-axis and propagating along the x-axis. This was done in order to best describe the measured complex focal spot of PETAL, which is composed of a central, intense, spot, surrounded by low-intensity extended wings (see Fig.1 in Ref. [49]). The central component of the laser spot was modeled by a Gaussian having a FWHM width of 20 μm and a dimensionless field strength of $a_L = eE_L/m_e c\omega_L = 1.1$. The wings were modeled by a Gaussian with a 130 μm FWHM width and a dimensionless field strength of $a_L = 1.3$. The cumulated maximum laser intensity was of 8×10^{18} Wcm^{-2} [49].

The target consisted of a semi-transparent aluminum (Al) preplasma and an overcritical plastic (CH) plasma (5 μm thick). Henceforth, $n_c = m_e\epsilon_0\omega_L^2/e^2$ (ω_L is the laser frequency, m_e the electron mass, e the elementary mass and ϵ_0 the vacuum permittivity) will denote the critical density beyond which the laser can no longer propagate in the plasma. For the $\lambda_L = 1$ μm wavelength of the PETAL laser pulse, one has $n_c = 1.1\times10^{21}$cm^{-3}. Based on hydrodynamic-radiative simulations [50], the electron density profile of the preplasma was taken to evolve as $n_e(x) = 5\,n_c\exp(5.45(x/150)^{0.29})$, where the longitudinal position x is here expressed in μm units. The minimum and maximum density values were set to 0.02 n_c and 5 n_c. The latter maximum density ($5n_c$), which also characterizes the uniform CH layer, was chosen such that it is high enough to accurately represent the absorption of the laser light and low enough to relax the constraints on the numerical discretization. The Al, C and H ions were assumed fully ionized, and initialized at a 10 eV temperature. The ionic species Al^{13+}, C^{6+}, H^+ and the electrons were represented with 4, 4, 8 and 32 macro-particles per cell, respectively. Coulomb collisions between the plasma particles were neglected. The laser wave impinged normally onto the plasma. Absorbing boundary conditions were used for both particles and fields. The simulation domain, of $L_x \times L_r = 318\ \mu$m$\times 163\ \mu$m dimensions, was discretized with a $\Delta x = \Delta r = 32$ nm mesh size. The simulation was run during a $\sim$ 3.4 ps integration time.

With the above parameters, proton acceleration proceeds from the standard TNSA mechanism [33,34]. During the interaction, the laser wave propagates through the extended undercritical preplasma while driving the electrons to relativistic energies through various processes. These have been examined in detail by some of us in a recent study [49], which revealed the importance of stochastic electron heating as a result of stimulated laser backscatter and laser filamentation in the preplasma.

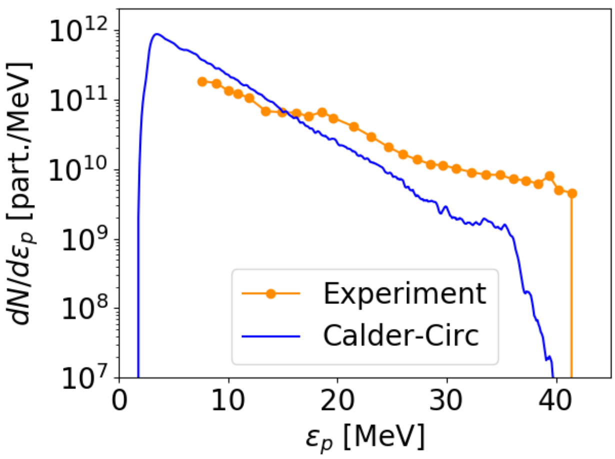

Figure 5: Proton spectrum from the CALDER-CIRC simulation using the LMJ-PETAL laser parameters (blue curve). An experimental proton spectrum obtained at LMJ-PETAL (see text for details) is plotted as orange dots.

After traversing the target, the laser-generated hot electrons form a negatively charged cloud at the backside. The associated electrostatic field then accelerates the plasma ions in the $+x$ direction. Figure 4 displays the longitudinal phase space of the protons as measured at $t = 3.4$ ps. The proton distribution exhibits a linear shape typical of TNSA, extending over $\sim$ $100\ \mu$m longitudinally and (from analysis of the $x - r$ proton density map) $\sim 300\ \mu$m transversely. The corresponding energy spectrum of the protons is plotted in Figure 5. It shows a decreasing exponential shape characteristic of TNSA, with a cutoff energy of $\sim$ 37 MeV.

To support the validity of our approach, we compare in Figure 5 the proton distribution predicted by CALDER-CIRC to an experimental one, which was recorded by us at LMJ-PETAL. It was measured with the CRACC diagnostic, which uses a radiochromic film stack as detector; the spectrum is here shown after angular integration onto the whole surface of the films [51]. In this shot, the PETAL laser irradiated a $7\ \mu m$ thick titanium foil with a pulse of $960\ fs$ duration, $354\ J$ energy and $\sim 5.3\times10^{18}\ Wcm^{-2}$ intensity, i.e., parameters relatively close to those of the simulation. Although the experimental proton spectrum is characterized by a harder slope and a larger cutoff energy ($\sim 42\ MeV$) than the simulated spectrum, the two curves agree fairly well with each other. This result is particularly satisfactory given the above simplifications made to the simulation in order to handle the spatiotemporal scales of the experiment. It should be noted that the experimental cutoff energy represents the last recorded point on the RCF stack although there were more

RCFs in the stack); such sharp cutoffs are common features of TNSA-accelerated proton beams.

3.2 Proton acceleration at the 0.6-6 PW Apollon laser facility

Proton acceleration using Apollon was simulated in 2D Cartesian geometry with the CALDER PIC code. The Apollon pulse was modeled as a $0.8\,\mu$m wavelength Gaussian electromagnetic wave linearly polarized along the (in-plane) y-axis, with 20 fs FWHM duration and $5\,\mu$m FWHM transverse size. We considered two operating regimes of the Apollon laser, characterized by a peak intensity of 2×10^{21} Wcm^{-2} (0.6 PW regime) and 2×10^{22} Wcm^{-2} (6 PW regime), respectively, see Table 2. Note that the temporal profile of the laser pulse is truncated at twice its FHWM duration ahead from the peak, i.e. the laser is switched on at that time. This starting point is chosen since it corresponds to an intensity that is 10^{-5} times the peak value. This ratio is close to what can be achieved using plasma mirrors as ultrafast switches, allowing one to virtually eliminate any ionizing light in the laser pulse prior to that level [52]. In practice, however, modulations in the pulse spectrum [37] could lead to the laser temporal profile deviating from the perfect Gaussian shape that we assume here. This may induce premature expansion of the target surface, hence affecting the irradiation conditions at the pulse maximum and thus the overall performance of the target. This will have to be taken in consideration, using experimental data for the laser temporal profile, when carefully planning experimental campaigns at maximum power.

The target was a thin, solid-density CH foil with sharp gradients. It was assumed to be fully ionized (yielding an electron density of $n_e = 200n_c$) and initialized at a temperature of 100 eV. Its thickness l was chosen based on the parametric simulation study of Ref. [29]. The optimum foil thickness for RPA by femtosecond laser pulses was found to be $l_{opt} \simeq 0.5a_L(n_c/n_e)\lambda_L$. In the 0.6 PW (resp. 6 PW) regime, corresponding to $a_L = 30$ (resp. $a_L = 96$), we chose $l = 64$ nm (resp. $l = 192$ nm), close to $l_{opt} = 60$ nm (resp. $l = 192$ nm). Each of the plasma constituents (C^{6+}, H^+, electrons) was modeled by 100 macro-particles per cell. The laser pulse interacted at normal incidence with the target. Absorbing boundary conditions were enabled for the fields and particles. The simulation domain was set to $L_x\times L_y = 40\times50\,\mu\text{m}^2$ at 0.6 PW ($56\times 96\,\mu\text{m}^2$ at 6 PW) with a spatial resolution $\Delta x = \Delta y = 3.2$ nm.

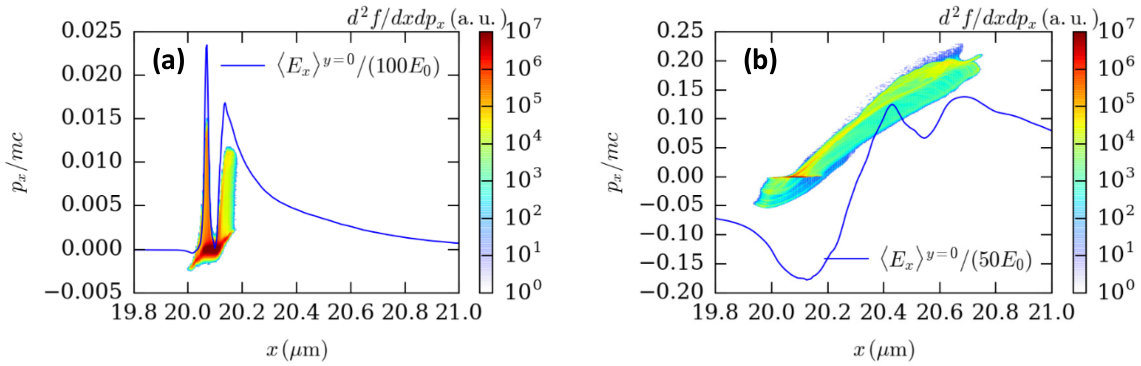

Figure 6: Proton acceleration using the 0.6 PW Apollon laser parameters: $x - p_x$ proton phase spaces at (a) $t = -20\,fs$ and (b) $t = +4\,fs$ (here $t = 0$ corresponds to the on-target laser pulse maximum). The blue line is the laser-cycle-averaged longitudinal electric field, $\langle E_x\rangle$, normalized to (a) 100 E_0 or (b) $50E_0$ for readability ($E_0 = 3.2\times10^{12}\ Vm^{-1}$).

The proton acceleration dynamics is illustrated by the longitudinal proton phase spaces shown at two successive times in Figure 6 and Figure 7 for the 0.6 PW and 6 PW irradiation cases, respectively. In each panel is also plotted (in blue) a lineout (along the laser axis) of the accelerating longitudinal electric field $\langle E_x \rangle$ (here $\langle \;\; \rangle$ indicates an average over the laser cycle). This field is normalized (in units of $E_0 = 3.2\times10^{12}$ Vm^{-1}) to fit within the p_x-axis of the phase space.

At time $t = -20$ fs (here the time origin $t = 0$ is when the laser maximum reaches the target), see panels (a) in Figure 6 and Figure 7, proton acceleration originates from both RPA and TNSA [12,34], as demonstrated by the two $\langle E_x \rangle$ peaks at the front and rear sides of the target. At the front side, the electrons are pushed and compressed by the laser's ponderomotive force. The ensuing charge separation generates an electrostatic field $\langle E_x \rangle \simeq 2E_0$ at 0.6 PW ($\simeq 10E_0$ at 6 PW), which, in turn, accelerates the front-side protons in the forward direction. These RPA protons have then reached a longitudinal momentum $p_x/m_i c \simeq 0.015$ ($\simeq 0.06$ at 6 PW). Simultaneously, the backside protons have started expanding towards vacuum due to TNSA triggered by the fast electrons. The associated electric field $\langle E_x \rangle \simeq 1.5E_0$ ($\simeq 3E_0$ at 6 PW), however, turns out to be weaker than the one induced by the radiation pressure (especially at 6 PW). At this early stage of the interaction, the maximum momentum of the TNSA protons is of $p_x/m_i c \simeq 0.0011$ ($\simeq 0.02$ at 6 PW).

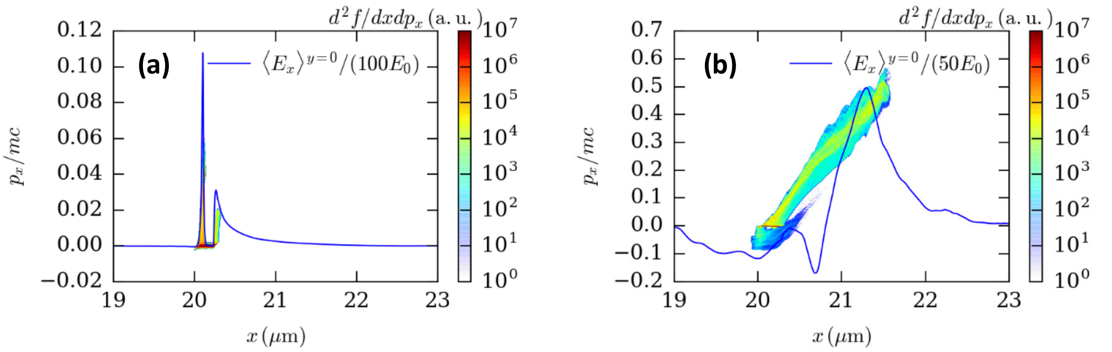

Figure 7: Proton acceleration using the 6 PW Apollon laser parameters: $x - p_x$ proton phase spaces at (a) $t = -20\,fs$ and (b) $t = +4\,fs$ (here $t = 0$ corresponds to the on-target laser pulse maximum). The blue line is the laser-cycle-averaged longitudinal electric field, $\langle E_x \rangle$, normalized to (a) $100\ E_0$ or (b) $50E_0$ for readability ($E_0 = 3.2\times10^{12} Vm^{-1}$).

At $t = +4$ fs [panels (b) in Figure 6 and Figure 7], the RPA protons have caught up with the TNSA protons, an the two previously observed field structures have merged into a single accelerating structure. Importantly, the expanding, lower-density plasma has then turned transparent to the central part of the laser pulse. This causes the electrons to be further heated and the accelerator field strength to be boosted to $\langle E_x \rangle \simeq 7.5\ E_0$ at 0.6 PW and $\langle E_x \rangle \simeq 25\ E_0$ at 6 PW), which, in both cases, represents about a quarter of the laser field amplitude.

As a result of this sequence of processes, the protons eventually attain high cutoff energies ($\simeq 115$ MeV at 0.6 PW and $\simeq 660$ MeV at 6 PW) as demonstrated by the energy spectra displayed in Figure 8(a,b). Note that these spectra are recorded when the protons reach the right-hand side of the box: their spatial distribution then has a $\sim 20 - 30\ \mu m$ transverse size, comparable with the travelled distance. The electrostatic field seen by the fastest protons should therefore be relatively well captured by our 2D simulation. We acknowledge, however, that the combination of a 2D geometry and laser p-polarization likely leads to a significant overestimation of the electron heating, and hence of the accelerator field compared to a real-world 3D configuration [53]. This, on top of the idealized temporal laser profile and target conditions (i.e., preplasma formation was neglected) we considered is bound to degrade the performance in the experiments compared to our simulation results.

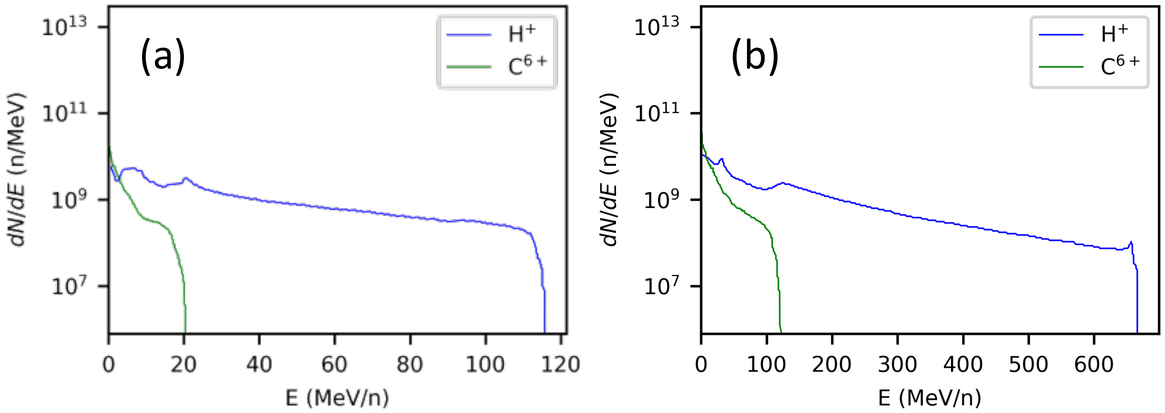

Figure 8: PIC-simulated proton spectra using the (a) 0.6 PW and (b) 6 PW Apollon laser parameters. In panel (a), the integrated number of protons above 10 MeV is of ~10^{11}, corresponding to a laser-to-proton energy conversion efficiency of ~5%. In panel (b), there are 5×10^{11} protons above 20 MeV, corresponding to a ~12% conversion efficiency.

4. Monte Carlo simulations of neutron generation

In the CALDER simulations, the properties (statistical weight, position, momentum, time of arrival) of the macro-protons crossing a virtual detector plane near the right-hand side of the simulation box were all recorded. The resulting output files contained between about 10^5 (PETAL) and 10^7 (Apollon) macro-protons. The proton distributions obtained from the 2D Apollon simulations had to be post-processed in order to be used as input in the FLUKA 3D Monte Carlo code. To this purpose, they were converted into cylindrically symmetric distributions. Specifically, the position and momentum of each macro-proton were rotated around the x-axis by a random azimuthal angle. Moreover, the transverse density profile of the proton distribution was interpreted as a radial density profile: the statistical weight of each macro-proton (a linear density in a 2D simulation) was thus multiplied by its transverse radius to obtain a dimensionless quantity, corresponding to the number of physical protons represented by the macro-proton. These numbers are reflected in the spectra shown in *Figure 8*, and are further detailed below.

The convertor target was taken to be a lead cylinder of fixed 5-cm radius and varying length ($10\ \mu m \leq l \leq 10$ cm), located 0.5 cm behind the proton-generating target. To get good statistics on the simulated events, we carried out 1000 independent Monte Carlo simulations for each set of initial conditions. Only those neutrons crossing the target rear side were characterized.

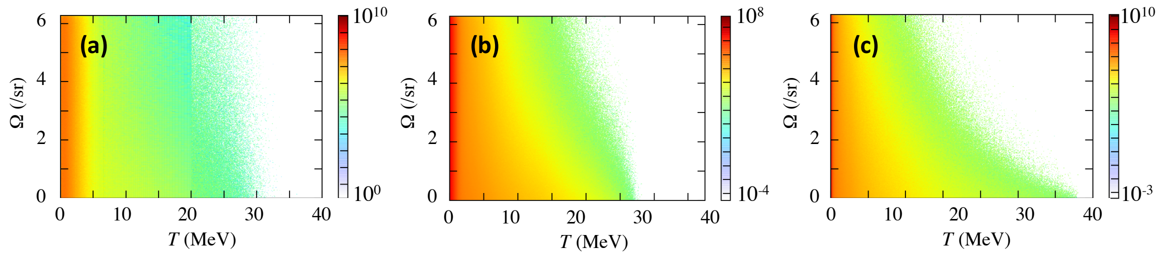

Figure 9: Energy-angle spectrum of the neutrons escaping from a 0.3 mm thick Pb converter target. (a) The incident proton beam is that of the LMJ-PETAL PIC simulation. (b) Same with the 0.6 PW Apollon laser parameters (c) Same with the 6 PW Apollon laser parameters.

Figure 9 displays the energy-angle spectrum of the outgoing neutrons from a 0.3 mm thick converter Pb target as predicted by FLUKA in the LMJ-PETAL (a) and 0.6-6 PW Apollon (b,c) cases. Overall, the neutron energy spectra show an exponentially decreasing shape up to a maximum energy close to that of the incident protons. This is more clearly seen in Figure 12.b, obtained from angular integration of the spectra of Fig. 9. It is worth noting that the lower-energy part of the neutron distribution is essentially isotropic, while its higher-energy part is preferentially emitted in the initial direction of the proton beam.

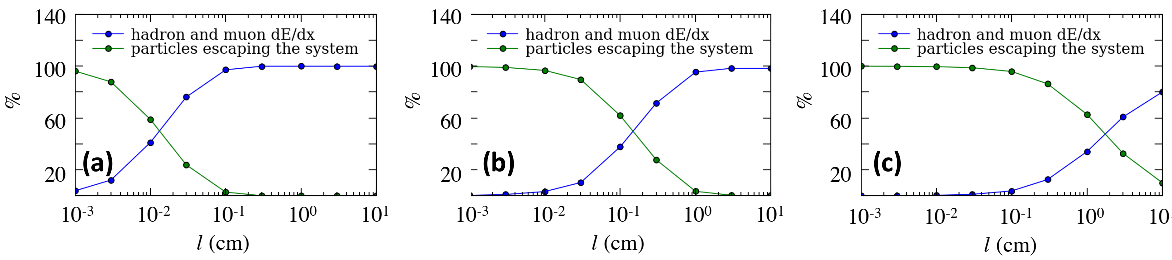

Figure 10: Energy fraction of the incident protons dissipated by nuclear reactions (blue) and transmitted through the target (green), as a function of the thickness l of the Pb converter target. Panels (a), (b) and (c) correspond, respectively, to the LMJ-PETAL, 0.6 PW Apollon and 6 PW Apollon lasers.

Figure 10 plots, as a function of the Pb target length l, the fraction of kinetic energy lost by the primary protons through nuclear reactions (blue curves) and that transmitted through the target (green curve). In the PETAL case, the proton beam energy is wholly dissipated for $l \geq 0.1$cm. In the 0.6 PW Apollon case, this takes place for $l \geq 1$ cm, while in the 6 PW case, the absorption is limited to $\sim 80\%$ at $l = 10$ cm.

Figure 11 (a) shows how the total number (per unit solid angle) of outgoing neutrons varies with l. Under the LMJ-PETAL conditions, the neutron number is seen to rise with l up to $l \simeq 0.1$ cm and to saturate at a $\sim 10^8$ n level in the range $0.1 \leq l \leq 3$ cm, before dropping at larger l as a result of reabsorption. In the 0.6 PW and 6 PW Apollon cases, due to higher proton energies, saturation occurs in thicker targets, namely, at $\sim 5\times10^8$ n for $1 \leq l \leq 3$ cm and at $\sim 10^{11}$ n for $3 \leq l \leq 10$ cm , respectively (the plateau observed at 6 PW may actually extend beyond the range of thicknesses considered here). These trends are consistent with the evolution of the dissipated proton energy as discussed above. Interestingly, the neutron yield is predicted to be quite similar for the LMJ-PETAL and 0.6 PW Apollon lasers. At first glance, this result may seem surprising given that LMJ-PETAL generates about 50 times more fast protons than 0.6 PW Apollon ($\sim 5\times10^{12}$ in a $2 - 40$ MeV energy range vs. $\sim 10^{11}$ in a $10 - 120$ MeV range) due to its relatively large spot size and long pulse duration. Yet the lower yield of protons achieved at 0.6 PW Apollon is compensated for by their higher cutoff energy that increases their neutron generation efficiency. Such enhancement is even more dramatic using the 6 PW Apollon parameters, in which case a sharp rise in the proton energies is observed. The $\sim 5\times10^{11}$ protons then produced above 20 MeV are predicted to translate into a two orders of magnitude higher neutron yield.

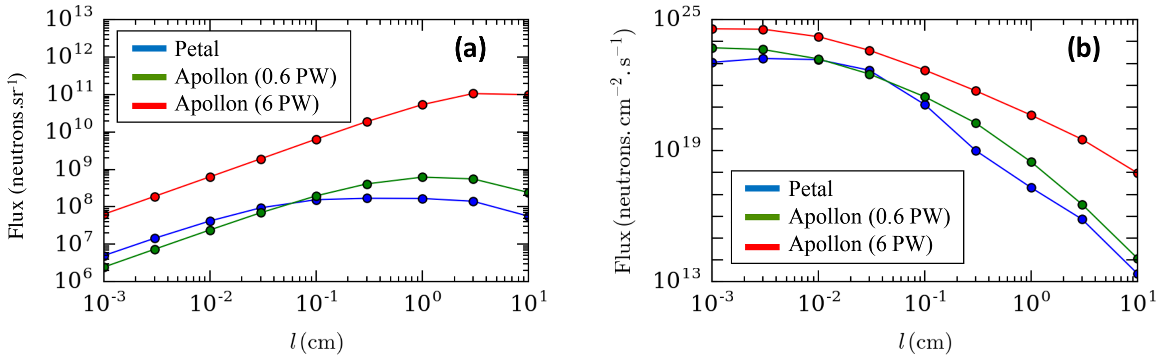

Figure 11: (a) Number (normalized to unit solid angle) and (b) maximum flux of the neutrons crossing the rear side of the Pb converter target, as a function of its thickness l. The incident proton beam is that predicted by PIC simulations in the LMJ-PETAL and 0.6-6 PW Apollon cases, as labeled.

Figure 11 (b) plots the corresponding variations in the maximum neutron flux at the backside of the Pb target. Note that FLUKA takes account of the time of injection of each proton into the convertor, so that the temporal profile of the total neutron flux across a given surface can be computed. The maximum flux appears to culminate in $l \lesssim 100\ \mu$m targets and to drop in increasingly thick targets. Values in excess of $\sim 1{\times}10^{23}$n cm^{-2} s^{-1} are expected at LMJ-PETAL and 0.6 PW Apollon, while a maximum flux as high as $\sim 4{\times}10^{24}$n cm^{-2}s^{-1} is found with the 6 PW Apollon parameters. This trend results from the increase in duration and the transverse size of the neutron distribution when the converter target is made thicker These variations originate from the energy dispersion of the incident proton beam (which leads to an elongation of the proton beam, and therefore of the generated neutron beam) as well as from elastic scatterings of both the protons and neutrons throughout the target (which mainly account for the transverse size of the neutron source). The temporal dependence of the neutron flux is illustrated in Figure 12(a) for LMJ-PETAL. It is observed that upon thickening the target from $l = 10\ \mu$m to 1 cm, the neutron pulse is lengthened from $\sim$ 3 ps to $\sim$ 6 ns. The correlation between the neutron source duration and transverse size is clearly shown in Figure 13. The three laser configurations give rise to a similar behavior: very compact neutron sources, of a few ps duration and $\sim 50 - 100\ \mu$m width only, are expected from $l \leq 100\ \mu$m Pb targets, which evolve into a few ns-long and cm-wide sources when cm-thick Pb targets are employed.

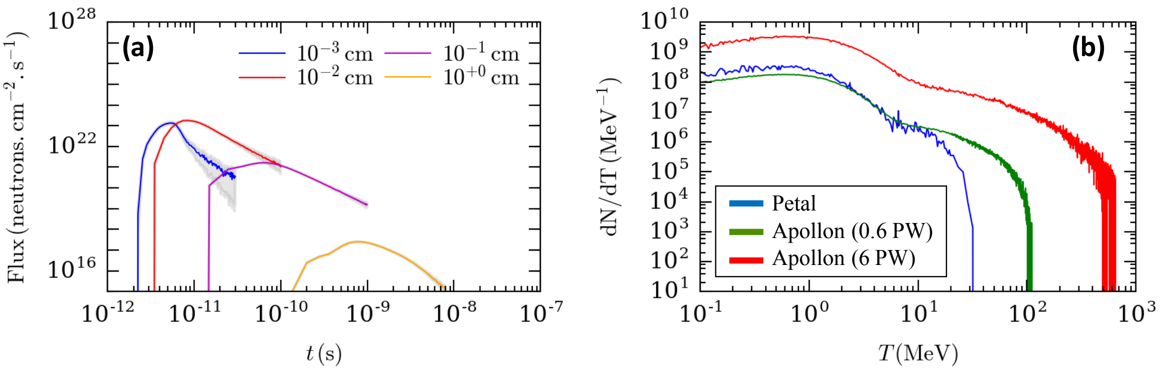

Figure 12: (a) Time-dependent neutron flux across the Pb converter backside for the LMJ-PETAL parameters. (b) Neutron energy spectra from a $l = 0.3$ mm Pb target in the LMJ-PETAL and 0.6-6 PW Apollon cases.

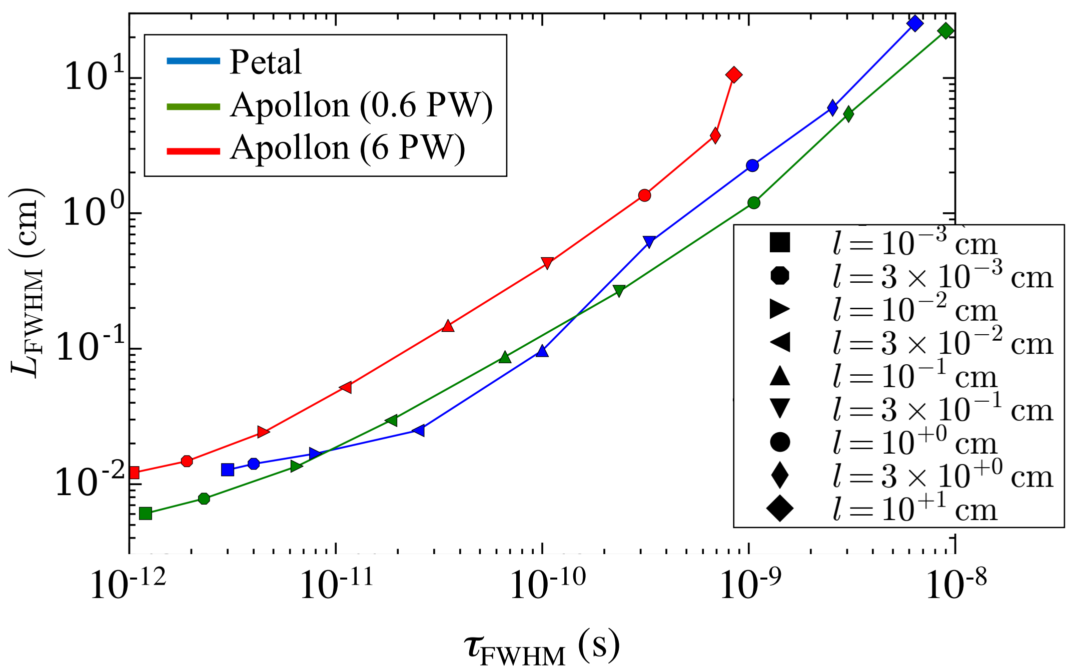

Figure 13: Transverse size vs duration of the simulated neutron beam in the LMJ-PETAL, 0.6 PW Apollon and 6 PW Apollon cases, and for various thicknesses, as indicated.

5. Discussion and summary of the properties of simulated neutron sources

We have here assessed the possibility of exploiting spallation reactions to generate high-flux neutron sources using PW-class lasers as the primary drivers. We have tested this scenario by combining two simulation codes, the first to simulate the proton generation by the laser, the second to simulate the neutron generation in a lead converter. Most notably, our results highlight the interest of using ultraintense femtosecond laser pulses to push the maximum proton energy. In particular, irradiation at the 6 PW level using Apollon, although yet untested experimentally, should produce protons beyond the 100 MeV threshold, that is, well above the current performance of higher-energy picosecond lasers such as the 0.5 PW LMJ-PETAL system. Such high proton energies translate into much larger neutron multiplicity from the converter targets, and therefore allow multi-PW short-pulse lasers to make up for their lower proton output.

Regarding the quantitative accuracy of our study, satisfactory agreement was demonstrated in the LMJ-PETAL case between an experimental proton spectrum and that obtained from a quasi-3D PIC simulation. While, as of now, such a comparison cannot be made in the Apollon setting, since the facility is still undergoing commissioning [55], we acknowledge the limitations of our 2D PIC simulations, and the fact that they may appreciably overestimate the proton cutoff energy (particularly in the 6 PW regime) as claimed by previous works [53]. This leaves room for a refined (but much more computationally demanding) simulation study based on 3D simulations, and using more realistic (i.e. non-Gaussian) temporal laser profiles [37], to be carried out in the future.

To conclude, we note that the $> 10^{23}\ \mathrm{n\ cm^{-2}s^{-1}}$ peak neutron fluxes predicted by our numerical study could be appropriate to laboratory studies of *r*-process nucleosynthesis. In particular, the short duration (in the ps-ns range) of the neutron source (shown in Figure 12.a and Figure 13) is adequate to perform nucleosynthesis experiments, since the β-decay of the created isotopes resulting from multiple neutron absorption occurs over much longer (> ms) timescales [54]. Beyond the practical achievement of such high instantaneous flux, which we will be soon able to verify using the Apollon laser facility [55], and other multi-PW facilities like ELI, an evaluation of the overall amount of isotopes that could be produced per laser shot or in a cumulative mode (over several shots) needs to be conducted using presently available, i.e. theoretically estimated, cross sections; this is an ongoing task that will be the focus of a separate publication.

Acknowledgements

This work was supported by the European Research Council (ERC) under the European Union's Horizon 2020 research and innovation program (Grant Agreement No. 787539). It was also supported by Grant ANR-17-CE30-0026-Pinnacle from Agence Nationale de la Recherche. We acknowledge GENCI, France, for awarding us access to HPC resources at TGCC/CCRT (Allocation No. A0010506129). We also acknowledge the support from the Extreme Light Infrastructure Nuclear Physics (ELI-NP) Phase II, a project co-financed by the Romanian Government and the European Union through the European Regional Development Fund - the Competitiveness Operational Programme (1/07.07.2016, COP, ID 1334), and by the project ELI−RO−2020−23 funded by IFA (Romania). The PETAL laser was designed and constructed by CEA under the financial auspices of the Conseil Régional d'Aquitaine, the French Ministry of Research, and the European Union. The CRACC diagnostic was designed and commissioned on the LMJ-PETAL facility as a result of the PETAL+ project coordinated by University of Bordeaux and funded by the French Agence Nationale de la Recherche under grant ANR-10-EQPX-42-01. The LMJ-PETAL experiment presented in this article was supported by Association Lasers et Plasmas and by CEA. The diagnostics used in the experiment have been realized in the framework of the EquipEx PETAL+ via contract ANR-10-EQPX-0048.

REFERENCES

[1] I. Obodovskiy, *Radiation: Fundamentals, Applications, Risks, and Safety* (Elsevier, 2019), Pages 289-292.
[2] O. Hallonsten and T. Kaiserfeld, *Between Making and Knowing* (2020, World Scientific), pp. 553-560.
[3] R. Garoby et al., *The European Spallation Source Design*, Phys. Scr. **93**, 014001 (2018)
[4] D. Filges and F. Goldenbaum, *Handbook of Spallation Research: Theory, Experiments and Applications* (2009, Wiley)
[5] A. Alejo, H. Ahmed, A. Green, S. R. Mirfayzi, M. Borghesi, and S. Kar, *Recent advances in laser-driven neutron sources*, Il Nuovo Cimento **38C**, 188 (2016).
[6] L. J. Perkins, B. G. Logan, M. D. Rosen, M. D. Perry, T. Diaz de la Rubia, N. M. Ghoniem, T. Ditmire, P. T. Springer, and S. C. Wilks, *The investigation of high intensity laser driven micro neutron sources for fusion materials research at high fluence*, Nucl. Fusion **40**, 1 (2000).

[7] R. Loveman, J. Bendahan, T. Gozani, and J. Stevenson, *Time of flight fast neutron radiography*, Nucl. Instrum. Methods Phys. Res. B **99**, 765 (1995).
[8] D. P. Higginson, J. M. McNaney, D. C. Swift, T. Bartal, D. S. Hey, R. Kodama, S. Le Pape, A. Mackinnon, D. Mariscal, H. Nakamura, N. Nakanii, K. A. Tanaka, and F. N. Beg, *Laser generated neutron source for neutron resonance spectroscopy*, Phys. Plasmas **17**, 100701 (2010).
[9] O. Noam, D. C. Gautier, N. Fotiades, A. Beck, I. Pomerantz, *Fast neutron resonance radiography with full time-series digitization*, Nucl. Instrum. Methods Phys. Res. A **955**, 163309 (2020).
[10] M. Roth, D. Jung, K. Falk, N. Guler, O. Deppert, M. Devlin, A. Favalli, J. Fernandez, D. Gautier, M. Geissel, R. Haight, C.E. Hamilton, B.M. Hegelich, R.P. Johnson, F. Merrill, G. Schaumann, K. Schoenberg, M. Schollmeier, T. Shimada, T. Taddeucci, J.L. Tybo, F. Wagner, S.A. Wender, C.H. Wilde, and G.A. Wurden. *Bright Laser-Driven Neutron Source Based on the Relativistic Transparency of Solids*, Phys. Rev. Lett. **110**, 044802 (2013).
[11] F. Wagner *et al., Maximum proton energy above 85 MeV from the relativistic interaction of laser pulses with micrometer thick* CH_2 *targets*, Phys. Rev. Lett. **116**, 205002 (2016)
[12] A. Higginson, R. J. Gray, M. King, R. J. Dance, S. D. R. Williamson, N. M. H. Butler, R. Wilson, R. Capdessus, C. Armstrong, J. S. Green, S. J. Hawkes, P. Martin, W. Q. Wei, S. R. Mirfayzi, M. Borghesi, R. J. Clarke, D. Neely and P. McKenna, *Near-100 MeV protons via a laser-driven transparency-enhanced hybrid acceleration scheme*, Nat. Comm. **9**, 724 (2018).
[14] J. Feng *et al., High-efficiency neutron source generation from photonuclear reactions driven by laser plasma accelerator*, HEDP **36**, 100753 (2020).
[15] I. Pomerantz, E. McCary, A. R. Meadows, A. Arefiev, A. C. Bernstein, C. Chester, J. Cortez, M. E. Donovan, G. Dyer, E. W. Gaul, D. Hamilton, D. Kuk, A. C. Lestrade, C. Wang, T. Ditmire, and B. M. Hegelich, *Ultrashort Pulsed Neutron Source*, Phys. Rev. Lett. **113**, 184801 (2014).
[16] AIEA report: https://www-pub.iaea.org/MTCD/Publications/PDF/te_1178_prn.pdf, page 50.
[17] S. R. Mirfayzi, A. Alejo, H. Ahmed, D. Raspino, S. Ansell, L. A. Wilson, C. Armstrong, N. M. H. Butler, R. J. Clarke, A. Higginson, J. Kelleher, C. D. Murphy, M. Notley, D. R. Rusby, E. Schooneveld, M. Borghesi, P. McKenna, N. J. Rhodes, D. Neely, C. M. Brenner, and S. Kar, *Experimental demonstration of a compact epithermal neutron source based on a high power laser*, Appl. Phys. Lett. **111**, 044101 (2017).
[18] M. Thoennessen, *Reaching the limits of nuclear stability*, Rep. Prog. Phys. **67**, 1187 (2004).
[19] S.N. Chen, F. Negoita, K. Spohr, E. d'Humières, I. Pomerantz, and J. Fuchs, *Extreme brightness laser-based neutron pulses as a pathway for investigating nucleosynthesis in the laboratory*, Matter Radiat. Extremes **4**, 054402 (2019).
[20] P. Hill and Y. Wu, *Exploring laser-driven neutron sources for neutron capture cascades and the production of neutron-rich isotopes*, Physical Review C **103**, 014602 (2021).
[21] T. Kajino et al., *Current status of r-process nucleosynthesis*, Prog. Part. Nucl. Phys. **107**, 109 (2019).
[22] J. J. Cowan, F.-K. Thielemann, and J. W. Truran, *The r-process and nucleochronology*, Phys. Rep. **208**, 267 (1991).
[23] I. S. Anderson, C. Andreani, J.M. Carpenter, G. Festab, G. Gorini, C.-K. Loong, R. Senesi, *Research opportunities with compact accelerator-driven neutron sources*, Phys. Rep. **654**, 1 (2016).

[24] C. Yeamans and B. Blue, *National ignition facility neutron sources*. https: //www.osti. gov / servlet / purl / 1458648. 62
[25] S. S. Bulanov, V. Yu. Bychenkov, V. Chvykov, G. Kalinchenko, D. W. Litzenberg, T. Matsuoka, A. G. R. Thomas, L. Willingale, V. Yanovsky, K. Krushelnick, and A. Maksimchuk, *Generation of GeV protons from 1 PW laser interaction with near critical density targets*, Phys. Plasmas **17**, 043105 (2010).
[26] J. Davis, and G. M. Petrov, *Generation of GeV ion bunches from high-intensity laser-target interactions*, Phys. Plasmas **16**, 023105 (2009).
[27] M. L. Zhou, X. Q. Yan, G. Mourou, J. A. Wheeler, J. H. Bin, J. Schreiber, and T. Tajima, *Proton acceleration by single-cycle laser pulses offers a novel monoenergetic and stable operating regime*, Phys. Plasmas **23**, 043112 (2016).
[28] E. d'Humières *et al., Longitudinal laser ion acceleration in low density targets: experimental optimization on the Titan laser facility and numerical investigation of the ultra-high intensity limit,* Proc. SPIE **9514**, 95140B (2015).
[29] A.V. Brantov, E.A. Govras, V. Yu. Bychenkov, and W. Rozmus*, Ion energy scaling under optimum conditions of laser plasma acceleration from solid density targets*, Phys. Rev. ST-AB **18**, 021301 (2015)
[30] A. V. Brantov, E. A. Govras, V. F. Kovalev, and V. Yu. Bychenkov*, Synchronized ion acceleration by ultraintense slow light*, Phys. Rev. Lett. **116**, 085004 (2016).
[31] A. A. Sahai *et al., Relativistically induced transparency acceleration of light ions by an ultrashort laser pulse interacting with a heavy-ion-plasma density gradient*, Phys. Rev. E **88**, 043105 (2013).
[32] H. Y. Wang *et al*., *High-energy monoenergetic proton beams from two-stage acceleration with a slow laser pulse,* Phys. Rev. ST-AB **18**, 021302 (2015).
[33] S. C. Wilks, A. B. Langdon, T. E. Cowan, M. Roth, M. Singh, S. Hatchett, M. H. Key, D. Pennington, A. MacKinnon, and R. A. Snavely, *Energetic proton generation in ultra-intense laser–solid interactions*, Phys. Plasmas **8**, 542 (2001).
[34] A. Macchi, M. Borghesi, and M. Passoni, *Ion acceleration by superintense laser-plasma interaction*. Rev. Mod. Phys. **85**, 751 (2013).
[35] D. A. Brown et al., "*ENDF/B-VIII.0: The 8th major release of the nuclear reaction data library with CIELO-project cross sections, new standards and thermal scattering data*", Nucl. Data Sheets 148, 1 (2018)
[36] A. Casner, T. Caillaud, S. Darbon, A. Duval, I. Thfouin, J.-P. Jadaud, J.-P. LeBreton, C. Reverdin, B. Rosse, R. Rosch, N. Blanchot, B. Villette, R. Wrobel, J.-L. Miquel, *LMJ/PETAL laser facility: Overview and opportunities for laboratory astrophysics*, HEDP **17**, 22 (2015).
[37] D. N. Papadopoulos, J. P. Zou, C. Le Blanc, G. Chériaux, P. Georges, F. Druon, G. Mennerat, P. Ramirez, L. Martin, A. Fréneaux, A. Beluze, N. Lebas, P. Monot, F. Mathieu and P. Audebert, *The Apollon 10 PW laser: experimental and theoretical investigation of the temporal characteristics*, High Power Laser Sci. Eng. **4**, e34 (2016).
[38] D. Batani *et al*., *Development of the PETAL laser facility and its diagnostic tools*, Acta Polytech. **53**, 103 (2013).
[39] J. Vyskočil, O. Klimo and S. Weber, *Simulations of bremsstrahlung emission in ultra-intense laser interactions with foil targets*, Plasma Phys. Control. Fusion **60**, 054013 (2018).
[40] J. Vyskočil, E. Gelfer, and O. Klimo, *Inverse Compton scattering from solid targets irradiated by ultra-short laser pulses in the* 10^{22}*–*10^{23} *W/cm*^{2} *regime,* Plasma Phys. Control. Fusion **62**, 064002 (2020).

[41] C. P. Ridgers, C. S. Brady, R. Duclous, J. G. Kirk, K. Bennett, T. D. Arber, A. P. L. Robinson, and A. R. Bell, *Dense Electron-Positron Plasmas and Ultraintense γ-rays from Laser-Irradiated Solids*, Phys. Rev. Lett. **108**, 165006 (2012)
[42] B. Rus, P. Bakule, D. Kramer, G. Korn, J. T. Green, J. Nóvak, M. Fibrich, F. Batysta, J. Thoma, J. Naylon, T. Mazanec, M. Vítek, R. Barros, E. Koutris, J. Hřebíček, J. Polan, R. Baše, P. Homer, M. Košelja, T. Havlíček, A. Honsa, M. Novák, C. Zervos, P. Korous, M. Laub, J. Houžvička, *ELI-Beamlines laser systems: status and design options*, Proc. SPIE **8780**, High-Power, High-Energy, and High-Intensity Laser Technology; and Research Using Extreme Light: Entering New Frontiers with Petawatt-Class Lasers, 87801T (2013).
[43] D. Doria, M.O. Cernaianu, P. Ghenuche, D. Stutman, K.A. Tanaka, C. Ticos and C.A. Ur, *Overview of ELI-NP status and laser commissioning experiments with 1 PW and 10 PW class-lasers*, J. Instrum. **15**, C09053 (2020).
[44] T. T. Böhlen, F. Cerutti, M. P. W. Chin, A. Fassò, A. Ferrari, P. G. Ortega, A. Mairani, P. R. Sala, G. Smirnov and V. Vlachoudis, *The FLUKA code: developments and challenges for high energy and medical applications.* Nucl. Data Sheets **120**, 211-214 (2014)
[45] A. Ferrari, P. R. Sala, A. Fassò, and J. Ranft, *FLUKA: a multi-particle transport code*, CERN-2005-10 (2005), INFN/TC_05/11, SLAC-R-773
[46] M. J. Berger, J. S. Coursey, M. A. Zucker, and J. Chang (2005), *ESTAR, PSTAR, and ASTAR: Computer programs for calculating stopping-power and range tables for electrons, protons, and helium ions* (version 1.2.3). National Institute of Standards and Technology, Gaithersburg, MD. http://physics.nist.gov/Star
[47] E. Lefebvre et al., *Electron and photon production from relativistic laser–plasma interactions*, Nuclear Fusion **43**, 629 (2003).
[48] A. F. Lifschitz et al., *Particle-in-Cell modelling of laser–plasma interaction using Fourier decomposition.* J. Comput. Phys. **228**, 1803 (2009).
[49] D. Raffestin *et al., Enhanced ion acceleration using the high-energy petawatt PETAL laser,* Matter Rad. Extremes **6**, 056901 (2021).
[50] E. Lefebvre et al., *Development and validation of the TROLL radiation-hydrodynamics code for 3D hohlraum calculations*, Nucl. Fusion **59**, 032010 (2018)
[51] I . Lantuéjoul, B. Vauzour, A. Duval, L. Lecherbourg, B. Marchet, C. Reverdin, B. Rossé, C. Rousseaux, J.-C. Toussaint, A. Chancé, D. Dubreuil, B. Gastineau, J.-C. Guillard, F. Harrault, D. Leboeuf, X. Leboeuf, D. Loiseau, A. Lotode, C. Pès, G. Boutoux, T. Caillaud, F. Granet, P. Prunet, T. Ceccotti, J. Fuchs, D. Batani, J.-E. Ducret, S. Hulin, K. Jakubowska, N. Rabhi, D. Raffestin, and L. Sérani, *SEPAGE: a proton-ion-electron spectrometer for LMJ-PETAL*, Proceedings Volume **10763**, Radiation Detectors in Medicine, Industry, and National Security XIX; 107630X (2018).
[52] A. Lévy et al., *Double plasma mirror for ultrahigh temporal contrast ultraintense laser pulses,* Opt. Lett. **32**, 310 (2007).
[53] D. J. Stark, L. Yin, B. J. Albright, and F. Guo, *Effects of dimensionality on kinetic simulations of laser-ion acceleration in the transparency regime*, Phys. Plasmas **24**, 053103 (2017).
[54] T. Suzuki *et al., β-decay Rates for Exotic Nuclei and r-process Nucleosynthesis up to Thorium and Uranium*, Astrophys. J., **859**, 133 (2018).
[55] K. Burdonov *et al., Characterization and performance of the Apollon Short-Focal-Area facility following its commissioning at 1 PW level,* Matter Rad. Extremes (in print 2021); http://arxiv.org/abs/2108.01336.